Applicable Analysis and Discrete Mathematics
available online at http://pefmath.etf.rs

Appl. Anal. Discrete Math. **19** (2025), 694–726.
https://doi.org/10.2298/AADM250214033I

FUZZY GRAPH AND NONLINEAR MODELS FOR MEDICAL IMAGE SEGMENTATION

Irma Ibrišimović, Nebojša M. Ralević, Bratislav D. Iričanin and Andrija Blesić*

Nonlinear analysis and graph theory form a unified framework for examining complex radiological image patterns. Pixel intensities are modeled as graph nodes, while edges represent spatial relations. Fuzzy graphs handle uncertainty, enabling flexible and robust segmentation. Entropy-based nonlinear methods enhance boundary detection and highlight structural irregularities. The framework improves identification of pathological regions and supports advanced image interpretation.

1. INTRODUCTION

Medical imaging plays a crucial role in modern medicine by providing accurate diagnoses and treatment planning. Radiological images including X-rays, Computed Tomography (CT), and Magnetic Resonance Imaging (MRI) often contain complex information that requires sophisticated processing methods.

The analysis of medical images poses significant challenges due to the complex structures and varying intensities present. Traditional methods often struggle to capture these nuances, which can lead to potential misinterpretations. This paper explores the integration of graph theory and fuzzy graphs as innovative approaches

*Corresponding author. Irma Ibrišimović
2020 Mathematics Subject Classification. 05C90,54E25, 68U10, 92C55E
Keywords and Phrases. Radiological Imaging, Graph and Fuzzy Theory, Nonlinear Analysis, Image Segmentation, Disease Progression Tracking

to enhancing the processing and interpretation of medical images. The main objectives include developing methodologies for constructing graphical representations of medical images and applying nonlinear techniques to extract crucial information.

The integration of nonlinear analysis and graph theory can significantly enhance the performance of existing image processing algorithms (see e.g. [**5**], [**12**], [**28**], [**10**], and related references cited therein). For instance, graph-based methods help precisely identify regions of interest within medical images, thereby improving segmentation accuracy. Moreover, nonlinear analysis methods enable a deeper understanding of structural and dynamic patterns within medical images. Approaches combining graph and computational methods have been specifically explored in radiological image analysis [**17**], which reinforces the relevance of our fuzzy-graph approach.

Recent studies have also emphasized the importance of optimal feature selection in medical image analysis. In [**17**] proposed a mathematical modelling approach for determining the optimal number of characteristic vectors in medical digital images, demonstrating its effectiveness in detecting structural changes in human liver tissue. Such an approach was effectively demonstrated in the study [**19**], where fuzzy distance-based filtering significantly improved image sharpness and quality across various types of noise [**21**].

By applying graph-based segmentation methods the accuracy of identifying and isolating regions of interest, such as tumors, can be improved thus having a critical influence on treatments type decisions [**12**]. Advanced approaches also facilitate the extraction of significant features from images, enhancing pattern recognition efficiency [**5**]. These techniques simplify data analysis while contributing to a better understanding of pathological processes, as demonstrated by [**28**].

In the context of image segmentation, noisy pixels may be replaced with better candidates based on the influence of surrounding pixels. The selection is guided by both the spatial fuzzy distance between pixels and differences in pixel brightness within the RGB color space, which is measured through an appropriate fuzzy metric. Such an approach was effectively demonstrated in the study [**21**], where fuzzy distance-based filtering significantly improved image sharpness and quality across various types of noise.

Consequently, the integration of fuzzy graphs and nonlinear analysis offers a robust and innovative framework for advancing the study and interpretation of complex medical images. By leveraging these methodologies, the interpretation of complex medical images can be significantly enhanced thereby leading to improved diagnostic accuracy.

In this paper, we first provide an overview of graph theory and the construction of graph-based models for image processing. This is followed by a discussion of fuzzy graph theory, highlighting its theoretical foundations and practical relevance. Subsequently, we present various image segmentation methods and the evaluation metrics used to assess their performance. Finally, the effectiveness of these approaches is demonstrated through experimental analysis on medical images, illustrating the potential of combining graph-theoretic and fuzzy methodologies for

accurate and efficient image interpretation.

2. GRAPH THEORY, FUZZY GRAPHS AND NONLINEAR ANALYSIS IN IMAGE PROCESSING

2.1 Graph Theory

Graph theory is a fundamental branch of discrete mathematical science that studies graphs that are a kind of relations respresentation, i.e. structures consisting of nodes (or vertices) and edges that connect these nodes. In our research we treat each pixel of the image as a node, while the edges represent relationships between pixels that are spatially close to each other. This representation allows us to conduct a more structured analysis of the internal patterns and relationships within images, such as organ contours, lesions, and other anatomical features.

Mathematically, we can define a graph as a ordered pair $G = (V, E)$, where V is the set of nodes (i.e. pixels) and E is the set of edges connecting some of these nodes. For example, if nodes v_i and v_j are connected by an edge, we can express this relationship as $(v_i, v_j) \in E$.

Before focusing on applications, we emphasize that throughout this work we specifically deal with *undirected graphs*. For clarity, let us remember the formal definition:

Definition 2.1. ***Undirected graph*** *is an ordered pair $G = (V, E)$, where $V = \{v_1, v_2, \ldots, v_n\}$ is the set of vertices, and E is the set of two-element subsets of V, called edges of the graph G (subsets $\{v_i, v_j\}$ such that $v_i, v_j \in V$ and $v_i \neq v_j$).*

The application of graph theory in medical imaging can be especially useful for enhancing our understanding of complex medical structures. For instance, by applying graph-based segmentation techniques, boundaries can be more accurately determined compared to traditional pixel-based methods. This paper is based on the relevant definitions provided in the book [**14**], although they are not explicitly presented in the text.

Digital image processing operates on sampled data from the underlying continuous light field. Each sample is called a **pixel** in 2D space, or a **voxel** in 3D space. Sampling is based on the concept of a lattice, which can be regarded as a regular tiling of space by a primitive cell. A lattice of dimension d (L_d) is a subset of the d-dimensional Euclidean space $\mathbb{R}^d$, defined as:

$$L_d = \{x \in \mathbb{R}^d \mid x = \sum_{i=1}^{d} k_i u_i;\ k_i \in \mathbb{Z}\} = U\mathbb{Z}^d,$$

where $u_1, \ldots, u_d \in \mathbb{R}^d$ form a basis of $\mathbb{R}^d$, and U is the matrix of column vectors.

A lattice in d-dimensional space is the set of all possible vectors that can be expressed as combinations of d linearly independent basis vectors with integer coefficients. The lattice points are given by Uk with $k^T = (k_1, \ldots, k_d) \in \mathbb{Z}^d$.

The unit cell of a lattice L_d with respect to the basis $u_1, \ldots, u_d$ is defined as

$$C = \{x \in \mathbb{R}^d \mid x = \sum_{i=1}^{d} k_i u_i,\ k_i \in [0,1]\} = U[0,1]^d,$$

where $[0,1]^d$ is the unit cube in $\mathbb{R}^d$. The volume of the cell C is $|\det U|$. The density of the lattice is defined as $\frac{1}{|\det U|}$, i.e., the number of lattice points per unit area [**14**].

The set $\{C + x \mid x \in \mathbb{R}^d\}$ of all lattice cells covers the entire space $\mathbb{R}^d$. The Voronoi cell of the lattice is called the *fundamental cell*, the translations of which cover the entire space. The Voronoi cell of a point contains all points that are closer to that point than to any other lattice point.

The boundaries of Voronoi cells are equidistant hyperplanes between neighboring lattice points. Two well-known 2D lattices are the rectangular lattice

$$U_1 = \begin{bmatrix} 1 & 0 \\ 0 & 1 \end{bmatrix}$$

and the hexagonal lattice

$$U_2 = \begin{bmatrix} \frac{\sqrt{3}}{2} & 0 \\ \frac{1}{2} & 1 \end{bmatrix}.$$

The most commonly used lattice in image processing and computer implementation is the rectangular sampling lattice derived from U_1. In image processing in 3D space, the sampling lattice is typically given by:

$$U_3 = \begin{bmatrix} 1 & 0 & 0 \\ 0 & 1 & 0 \\ 0 & 0 & k \end{bmatrix},$$

for some constant k, where the most common case is $k \geq 1$.

The most common way of using a graph to model image data is by identifying each vertex with a pixel or voxel and defining the edge structure in order to determine local neighborhoods for each vertex. Since the lattice defines a regular distribution of pixels, it is possible to construct a regular graph by connecting pairs of vertices that are within a fixed Euclidean distance of each other [**14**].

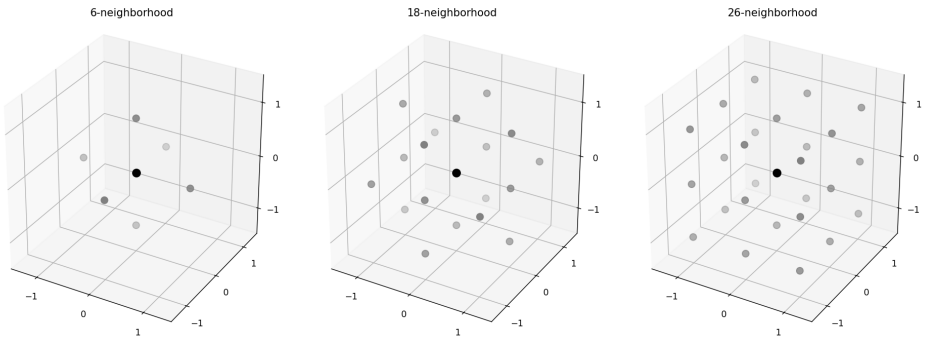

Figure 1: Illustration of different connectivity structures in a 3D lattice: 6-neighborhood, 18-neighborhood, 26-neighborhood

We define the Euclidean distance between nodes as $D(v_i, v_j) = \|x_i - x_j\|_2$, and the ball $B(v_i, r)$ includes all nodes within radius r from central node v_i.

Two proximity graphs are particularly useful, namely:

- **Delaunay Triangulation (DT)**: Connects two points v_i and v_j if there exists a circle (or sphere) passing through them that contains no other point inside. This triangulation maximizes the minimum angle between edges and is well-suited for capturing local structures in images. DT is dual to the Voronoi diagram, and its edges define meaningful neighborhoods for segmentation tasks.

- **Complete Graph (CG)**: Every pair of nodes is connected. While rarely used directly in image analysis due to complexity, CG serves as a conceptual model for measuring all possible similarities between pixels.

These graph models enable robust segmentation by taking into considerating spatial and intensity relationships, integrating prior anatomical knowledge as constraints within the graph structure (see e.g. [**22, 30**]).

2.2 Fuzzy Graph Theory

The development of fuzzy graph theory relies on the theoretical framework of fuzzy sets and fuzzy logic, as introduced in [**32**], providing the essential basis for modelling uncertainty in graphs. In fuzzy set theory, each element has a degree of membership, typically expressed as a value from the interval $[0, 1]$, rather than a crisp binary status of either belonging or not. A fuzzy set A in a space X is

formally defined by a membership function $\mu_A : X \to [0,1]$, where $\mu_A(x)$ indicates the degree to which element $x \in X$ belongs to the set A.

For notational simplicity, we will write (x, y) for an edge in an undirected graph (V, E), where $x, y \in V$. There is no need to consider loops, i.e., edges of the form (x, x), since we assume that our fuzzy relation is reflexive. A fuzzy graph is defined via a fuzzy relation p on a fuzzy subset σ of the set V. The function σ is called the *fuzzy vertex set* of the graph G, while μ is called the *fuzzy edge set* of G. Unless otherwise stated, we assume that the underlying set V is finite. For notational convenience, we will omit V and write simply $G = (\sigma, \mu)$.

Thus, in the most general case, both vertices and edges have membership values. However, in the special case where $\sigma(x) = 1$ for every $x \in V$, only the edges have fuzzy membership. In this case, the simplified notation $G = (\sigma, \mu)$ is used.

Definition 2.2 ([**18**]). *A fuzzy graph $H = (v, T)$ is called a **partial fuzzy subgraph** of a graph $G = (\sigma, \mu)$ if $v \subseteq \sigma$ and $T \subseteq \mu$.*

Definition 2.3. *A fuzzy graph $H = (P, v, T)$ is called a **fuzzy subgraph** of a graph $G = (\sigma, \mu)$ if the following conditions hold:*

- *$P \subseteq V(G)$ is the vertex set of the subgraph.*
- *$v : P \to [0,1]$ is the membership function assigning to each vertex $x \in P$ a membership degree $v(x)$, where $v(x) = \sigma(x)$ as in the fuzzy graph G.*
- *$T : P \times P \to [0,1]$ is the edge function of the subgraph, where $T(x, y) = \mu(x, y)$ for all $x, y \in P$.*

Extending this concept, a fuzzy graph allows uncertainty not only in the presence of vertices and edges, but also in the strength of connections between them. Prior to proceeding with the implementation, we will first present the necessary definitions provided in [**24**], that are crucial for our investigation.

Definition 2.4. *Let $G = (\sigma, \mu)$ be a fuzzy graph. The degree of a vertex u is given by the sum*

$$d_G(u) = d(u) = \sum_{u \neq v} \mu(u, v).$$

Definition 2.5. *Let $G = (\sigma, \mu)$ be a fuzzy graph with $|V| = n$ and $\mu = \{e_1, e_2, \ldots, e_m\}$. If $m_i = \mu(e_i)$ is the strength of the connection associated with the i-th edge, then*

$$\sqrt{2} \sum_{i=1}^{m} m_i^2 + n(n-1) \leq E(G) \leq \sqrt{2} \sum_{i=1}^{m} m_i^2.$$

Paths and Connectivity. A path P in a fuzzy graph $G = (\sigma, \mu)$ is a sequence of vertices $x_0, x_1, \ldots, x_n$, where x_0 and x_n may be equal and for every $1 \leq i \leq n$ we have $\mu(x_{i-1}, x_i) > 0$. Here, $n \geq 1$ is the length of the fuzzy path P. The consecutive pairs (x_{i-1}, x_i) are called the edges of the fuzzy path [**18**].

The diameter between two vertices $x, y \in V$, denoted as $\operatorname{diam}(x, y)$, is the length of the longest path that connects x and y. In [**4**] it is shown that if $\operatorname{diam}(x, y) = 1$, then $\mu_\infty(x, y) = \mu(x, y)$. Also, in [**4**] it is shown that if $\operatorname{diam}(x, y) = k$, then

$$\mu_\infty(x, y) = \bigvee\{\mu_i(x, y) \mid i = 1, 2, \ldots, k\}.$$

Here, the disjunction $\bigvee$ is taken over all path strengths $\mu_i(x, y)$ of paths connecting x and y of length $i = 1, 2, \ldots, k$. In fact, the algorithm for calculating μ_∞ is given in [**4**].

The strength of a path P is defined as $\bigwedge_{i=1}^{n} \mu(x_{i-1}, x_i)$.

In other words, the strength of a path is the weight of the weakest edge on the path. A vertex x can be considered a path. In this case, the path has the length equal to zero. If the path has length zero, it is convenient to define its strength as $\sigma(x_0)$.

It should be noted that any path of length $n > 0$ can also be defined as a sequence of edges (x_{i-1}, x_i), $1 \leq i \leq n$, that satisfy the condition $\mu(x_{i-1}, x_i) > 0$.

A partial fuzzy subgraph (μ, σ) is called connected if for all $x, y \in \operatorname{supp}(\sigma)$, we have $\mu_\infty(x, y) > 0$.

A path P is called a cycle if $x_0 = x_n$ and $n \geq 3$. Two vertices connected by a path are said to be connected. Clearly, the "connectivity" relation is an equivalence one. In fact, x and y are connected if and only if $\mu_\infty(x, y) > 0$ holds. The equivalence classes of vertices according to this relation are called the connected components of the given fuzzy graph. These represent its maximal connected partial fuzzy subgraphs. The strongest path connecting two vertices x and y has strength $\mu_\infty(x, y)$.

Example 2.1. *Let us consider an undirected fuzzy graph $G = (V, \mu)$, where*

$$V = \{a, b, c, d, e\}$$

and the edge membership values are defined as

$$\mu(a, b) = 0.8, \quad \mu(a, c) = 0.6, \quad \mu(b, d) = 0.7, \quad \mu(c, d) = 0.5, \quad \mu(d, e) = 0.9.$$

- *The path $P_1 = (a, b, d, e)$ has strength*

$$\bigwedge\{\mu(a, b), \mu(b, d), \mu(d, e)\} = \min(0.8, 0.7, 0.9) = 0.7.$$

- *The path $P_2 = (a, c, d, e)$ has strength*

$$\bigwedge\{\mu(a, c), \mu(c, d), \mu(d, e)\} = \min(0.6, 0.5, 0.9) = 0.5.$$

- *The diameter between vertices a and b is $\operatorname{diam}(a, b) = 1$, because the longest path between them contains only one edge.*

- *The diameter between vertices a and b is* $\operatorname{diam}(a, b) = 3$*, because the longest path $a \to c \to d \to b$ contains three edges.*

- *The connectivity strength between vertices a and e is*

$$\mu_\infty(a, e) = \bigvee\{0.7, 0.5\} = 0.7.$$

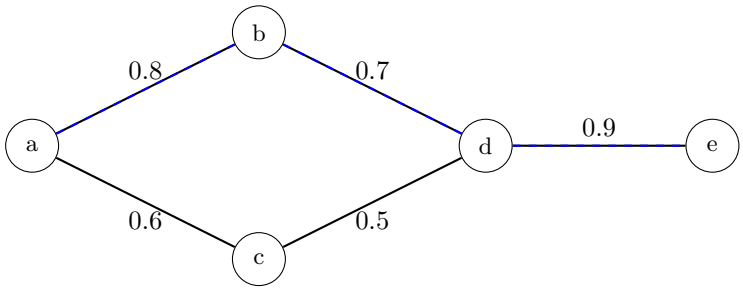

Figure 2: The example of a path in an undirected fuzzy graph $G = (\sigma, \mu)$

Clustering. Clustering, as applied to graph theory and fuzzy graphs, can be examined in detail in the book by Morderson et al. [**18**]. However, for our problem, we will focus on one of these clustering techniques, namely the ε-clustering. We apply the results to clustering analysis. We assume that a fuzzy graph $G = (\sigma, \mu)$ is given, where σ is the set of vertices (data points), and $\mu(u, v)$ is a quantitative measure of the similarity between two vertices u and v within the fuzzy graph. For $0 < \varepsilon \leq 1$, an ε-cluster in σ is a maximal subset $W \subseteq \sigma$ such that every pair of elements in W is mutually ε-reachable. Therefore, the construction of ε-clusters in σ is equivalent to finding all maximal strongly ε-connected fuzzy subgraphs of G.

Construction of ε-clusters:

1. Compute $\mu_1, \mu_2, \ldots, \mu_k$, where k is the smallest integer such that $\mu_k = \mu_{k+1}$.

2. Let $\mathcal{F} = \bigcup_{i=1}^{k} F_i$.

3. Construct F_i. Then, each element in F_i is a ε-cluster.

We may also define a ε-cluster in the set of vertices σ of the fuzzy graph $G = (\sigma, \mu)$ as a maximal subset $W \subseteq \sigma$ such that every element in W is ε-reachable from a special element $v \in W$. In this case, the construction of ε-clusters is equivalent to finding all maximal initial ε-connected fuzzy subgraphs of G. The Figure 3. below illustrates the resulting ε-clusters, where each color represents a maximal ε-connected subset of vertices according to the fuzzy graph $G = (\sigma, \mu)$.

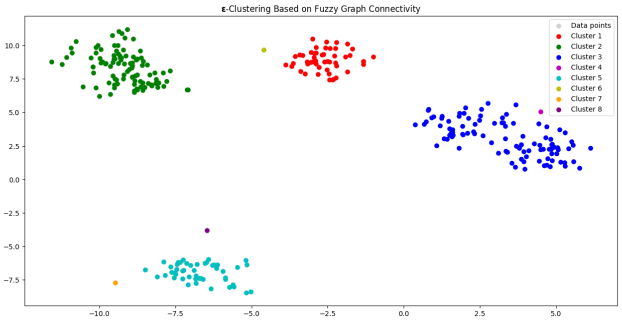

Figure 3: Example of ε-clustering based on fuzzy graph connectivity. Each color represents a maximal ε-connected cluster of data points. The similarity between points is defined by a fuzzy relation $\mu(u, v)$ and clusters correspond to strongly ε-connected subgraphs of the fuzzy graph $G = (\sigma, \mu)$.

The first figure (Figure 3) shows an example of ε-clustering for a single threshold. Each color represents a maximal ε-connected cluster of data points according to the fuzzy graph $G = (\sigma, \mu)$.

The second figure (Figure 4) illustrates the effect of varying the threshold ε on the clustering structure. Each subplot corresponds to a different value of ε, demonstrating how the number and composition of maximal ε-connected clusters change as the threshold varies. This visualization highlights the sensitivity of ε-clustering to the choice of the threshold parameter.

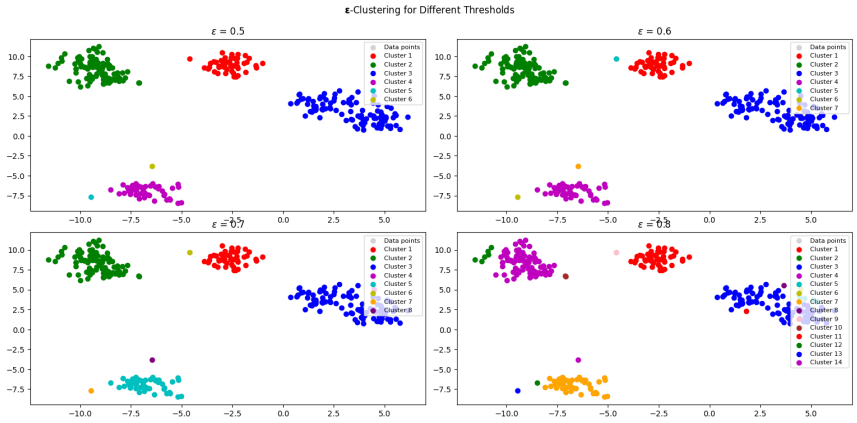

Figure 4: Illustration of ε-clustering for different thresholds. Each subplot corresponds to a specific value of ε, showing the maximal ε-connected clusters of data points according to the fuzzy graph $G = (\sigma, \mu)$. Colors represent distinct clusters for each ε.

3. IMAGE SEGMENTATION

Image segmentation is a fundamental and very challenging problem in the field of image processing, especially in medical imaging, where accurate delineation of anatomical and pathological structures is essential for diagnosis and treatment planning [**29, 20**]. Formally, let an image be represented as

$$I : \Omega \subset \mathbb{R}^2 \to \mathbb{R},$$

where Ω denotes the spatial domain of the image, i.e., the set of all pixel coordinates (x, y), and $I(x, y)$ represents the intensity value at pixel (x, y). The goal of segmentation is to partition the image domain Ω into disjoint regions

$$\{\Omega_1, \Omega_2, \ldots, \Omega_n\},$$

where each $\Omega_i \subset \Omega$ corresponds to a meaningful object or tissue type. These regions satisfy

$$\bigcup_{i=1}^{n} \Omega_i = \Omega, \quad \Omega_i \cap \Omega_j = \emptyset \text{ for } i \neq j.$$

Thresholding is a simple approach that segments the image based on intensity values. For a threshold T, the segmented image $S(x, y)$ is defined as

$$S(x, y) = \begin{cases} 1, & \text{if } I(x, y) \geq T, \\ 0, & \text{otherwise,} \end{cases}$$

where $S(x, y)$ is a binary map indicating whether the pixel (x, y) belongs to the object of interest, $I(x, y)$ is the original intensity, and T is a chosen threshold value [**11**].

Region-based methods, such as region growing, rely on spatial continuity. Starting from a seed pixel $s \in \Omega$, neighboring pixels (x, y) are added to the region Ω_i if their intensity satisfies

$$|I(x, y) - I(s)| < \delta,$$

where δ is a tolerance defining similarity. This ensures that regions are homogeneous in intensity and spatially connected [**7**].

Mathematical morphology employs a structuring element B to perform operations like dilation and erosion:

$$(I \oplus B)(x, y) = \max_{(u,v)\in B} I(x - u, y - v), \quad (I \ominus B)(x, y) = \min_{(u,v)\in B} I(x + u, y + v),$$

respectively where $(u, v) \in B$ denotes positions within the structuring element relative to its origin. Morphological gradients are often used to compute the image gradient

$$G(x, y) = \sqrt{\left(\frac{\partial I}{\partial x}\right)^2 + \left(\frac{\partial I}{\partial y}\right)^2},$$

where $G(x, y)$ is the gradient magnitude at pixel (x, y), and $\frac{\partial I}{\partial x}$, $\frac{\partial I}{\partial y}$ are partial derivatives along horizontal and vertical axes. In the Watershed algorithm, $G(x, y)$ is interpreted as a topographic surface, with local minima representing catchment basins, while Watershed lines define the boundaries between regions [**5, 31**].

Active contour models describe evolving curves $C(t)$ according to image-driven and smoothness forces:

$$\frac{\partial C}{\partial t} = F_{\text{image}} + \alpha F_{\text{smooth}},$$

where $C(t)$ is the curve at time t, F_{image} attracts the contour toward edges, F_{smooth} enforces contour regularity, and α is a weighting factor balancing these contributions [**8**].

Fuzzy C-means (FCM) clustering assigns a membership degree $u_{ik} \in [0, 1]$ to each pixel i for cluster k, ensuring

$$\sum_{k=1}^{c} u_{ik} = 1,$$

where c is the number of clusters. The objective function to minimize is

$$J_m = \sum_{i=1}^{N} \sum_{k=1}^{c} u_{ik}^m \|x_i - c_k\|^2,$$

with $m > 1$ being the fuzziness parameter, x_i the feature vector of pixel i, c_k the centroid of cluster k, and N the total number of pixels. Minimizing J_m assigns pixels to clusters based on similarity [**13, 26**].

Graph-based segmentation models the image as a weighted graph $G = (V, E)$, where nodes V correspond to pixels and edges E have weights w_{ij} representing similarity between pixels i and j. A common approach is normalized cut, defined as

$$Ncut(A, B) = \frac{cut(A, B)}{assoc(A, V)} + \frac{cut(A, B)}{assoc(B, V)},$$

where

$$cut(A, B) = \sum_{i \in A, j \in B} w_{ij}, \quad assoc(A, V) = \sum_{i \in A, j \in V} w_{ij},$$

and A, B are partitions of the graph. Here, $cut(A, B)$ measures the total weight between partitions, and $assoc(A, V)$ measures total connections from A to all nodes in the graph [**1, 6**].

More recently, deep learning approaches, such as U-Net and Feature Pyramid Networks (FPN), learn hierarchical features directly from images, achieving state-of-the-art segmentation performance [**23, 27**]. In this paper, we focus on exploring and analyzing the FPN method.

FPN is a deep learning architecture designed to extract multi-scale features for image segmentation. It constructs a top-down feature pyramid with lateral connections, merging high-level semantic information from deeper layers with spatially

rich features from shallower layers. Let C_l denote the feature map at the level l of backbone network. The fused feature map P_l is computed as

$$P_l = \mathit{Upsample}(P_{l+1}) + \mathit{Conv}(C_l),$$

where *Upsample* represents nearest-neighbor or bilinear upsampling, and *Conv* is a 1×1 convolution to reduce channel dimensions. This hierarchical feature fusion enhances precise localization while preserving semantic context, thereby improving segmentation performance across objects of varying scales.

In the following, we will apply all the previously described segmentation methods to demonstrate their performance and applicability. First, we will visually illustrate them on an example image from the comprehensive study [**20**], which serves as a methodological reference. Subsequently, we will apply the same methods to medical image, as presented in the paper [**9**]. This approach aims to show how different segmentation techniques, including Watershed, FCM, and region-based methods, can be effectively combined to extract regions of interest in complex medical images.

3.3 Evaluation Metrics for Segmentation

To quantitatively evaluate the performance of segmentation methods applied in this study, we employ similarity and overlap metrics commonly used in medical image analysis. One of the most widely adopted measures is the **Dice similarity coefficient** (DSC), also known as the Sørensen–Dice index [**25**].

Given a segmented region S produced by an algorithm and a ground truth region G (manually annotated), the Dice coefficient is defined as:

$$\mathrm{DSC} = \frac{2|S \cap G|}{|S| + |G|}, \tag{1}$$

where $|S|$ and $|G|$ denote the number of pixels (or voxels) in the respective regions, and $|S \cap G|$ is the number of pixels shared by both.

The DSC ranges from 0 to 1, where 0 indicates no overlap and 1 corresponds to perfect matching between the segmentation and the ground truth. This metric is particularly suitable for evaluating medical images with heterogeneous and complex structures as it accounts for both false positives and false negatives in the segmented region.

Following the methodological considerations highlighted by [**25**], special attention must be given to:

1. Ensuring consistent definitions of regions S and G, particularly in cases of partial volume effects or fuzzy boundaries.

2. Reporting DSC alongside other complementary metrics (e.g., Jaccard index) to provide a comprehensive evaluation of segmentation performance.

3. Considering object size variability to avoid bias in the evaluation of small vs. large anatomical structures.

In addition to the Dice similarity coefficient, we employ the **Jaccard index** (also known as the Intersection over Union, IoU) [**3**], which is defined as:

$$\text{Jaccard}(S, G) = \frac{|S \cap G|}{|S \cup G|}, \tag{2}$$

where $|S \cup G|$ denotes the total number of pixels present in either the segmented region S or the ground truth G. The Jaccard index ranges from 0 to 1, with higher values indicating better agreement. While similar to the Dice coefficient, the Jaccard index provides a slightly more stringent measure of overlap and is particularly useful when assessing the performance of segmentation methods on complex and irregular structures.

Both metrics complement each other: the Dice coefficient emphasizes the harmonic mean of precision and recall, whereas the Jaccard index directly measures the proportion of shared pixels relative to the total union of regions. By using these two metrics in conjunction we obtain a robust and comprehensive evaluation of segmentation quality.

To achieve a more complete assessment of segmentation results, we also consider additional cluster validity indices (CVIs) such as the **Fuzzy Silhouette Index** [**16**], **Davies–Bouldin Index** [**2**] and **Calinski–Harabasz Index** [**15**], which quantify intra-cluster compactness and inter-cluster separation. These indices are particularly relevant when fuzzy clustering techniques (e.g., FCM) or graph-based segmentations produce soft or overlapping regions.

In the subsequent analysis we will apply all segmentation methods under predefined parameters and evaluate their performance using the Dice coefficient, Jaccard index, and cluster validity indices. This ensures that both pixel-level accuracy and cluster-level consistency are quantitatively assessed, allowing for objective comparison across various methods and datasets.

In this study, the reference or ground truth masks were defined based on clearly identifiable regions in the input images, following the same methodology as in [**9**],[**20**]. For the standard grayscale image, the object of interest was manually delineated to serve as a reference region, while for the CT abdominal image the reference mask was constructed according to the visible anatomical boundary in the original scan. These masks were used for the evaluation of segmentation accuracy using Dice and Jaccard indices. It should be noted that the evaluation was conducted on a single representative image for each scenario, which nevertheless allows meaningful comparison of segmentation methods.

4. EXPERIMENTAL APPLICATION OF SEGMENTATION TECHNIQUES

In this section we present the experimental application of various image segmentation techniques on representative 2D grayscale images. The primary goal is

to evaluate and compare the performance of traditional, fuzzy, and graph-based methods in delineating regions of interest. Figures 5 and 6 illustrate the segmentation outcomes obtained by each of the methods.

The *original image* serves as a baseline for comparison. *Thresholding* segments the image based on intensity values, assigning pixels above a predefined threshold to the object class and the remainder to the background. *Region growing* leverages spatial continuity, expanding a region from a seed pixel by including neighboring pixels with intensity differences below a specified tolerance, thereby producing homogeneous and connected regions. *FPN* is a deep learning-based method that extracts multi-scale hierarchical features by combining high-level semantic information from deeper layers with spatially rich features from shallower layers, improving segmentation accuracy across objects of varying scales. *Watershed segmentation* interprets the image as a topographic surface where local minima correspond to catchment basins, and Watershed lines define boundaries between adjacent regions. *FCM* clustering assigns a membership degree to each pixel for multiple clusters, allowing for soft boundaries and capturing gradual transitions in intensity. The $\boldsymbol{\varepsilon}$*-clustering* method is applied as a graph-based approach, where pixels correspond to nodes and edges encode similarity based on intensity differences. The algorithm proceeds as follows:

1. Construct a fuzzy graph $G = (V, \mu)$ from the image, where each pixel is a node $v \in V$, and edge weights $\mu(u, v)$ represent intensity-based similarity between pixels u and v.

2. For a given threshold $0 < \boldsymbol{\varepsilon} \leq 1$, identify all maximal subsets of nodes $W \subseteq V$ such that every pair of nodes in W is ϵ-connected, i.e., mutually reachable with edge weights above $\boldsymbol{\varepsilon}$.

3. Assign each maximal $\boldsymbol{\varepsilon}$-connected subset W as a cluster representing a segmented region.

4. Repeat the process for all pixels until the entire graph is partitioned into $\boldsymbol{\varepsilon}$-clusters.

This algorithm allows segmentation to capture both spatial coherence and intensity similarity, producing clusters that represent meaningful regions in the image while maintaining connectivity information. The visualization highlights the strengths and limitations of each segmentation method, demonstrating differences in boundary precision, spatial coherence, and sensitivity to parameter selection. This comparative analysis provides a solid foundation for subsequent quantitative evaluation using clustering and segmentation metrics.

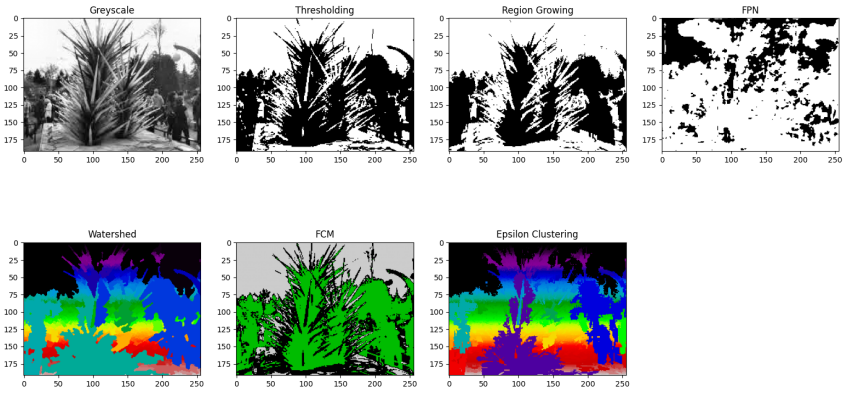

Figure 5: Segmentation results obtained using multiple techniques on the original image from the paper [**20**]: Greyscale image, Thresholding, Region Growing, FPN, Watershed, FCM, and ε-clustering.

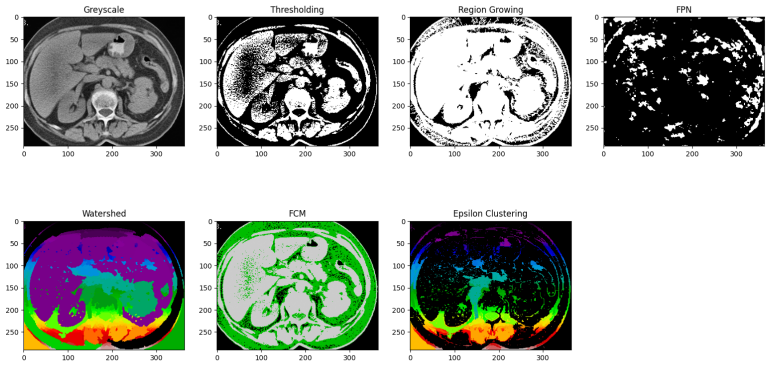

Figure 6: Segmentation results obtained using multiple techniques on a sample CT abdominal image [**9**]: Original image, Thresholding, Region Growing, FPN, Watershed, FCM, and ε-clustering. Each method highlights regions of interest with varying boundary precision and spatial coherence.

After presenting the general description of segmentation techniques, we fo-

cus on the parameters explored for each method. The objective of this analysis is to evaluate how varying key parameters affects segmentation quality and the delineation of regions of interest.

Thresholding: The threshold value determines the intensity level above which pixels are assigned to the foreground. Six different thresholds were tested:

$$T_1 = 0.2, \quad T_2 = 0.3, \quad T_3 = 0.4, \quad T_4 = 0.5, \quad T_5 = 0.6, \quad T_6 = 0.7.$$

Lower threshold values tend to include more background noise, while higher values may omit faint structures of interest.

Algorithm 1 Thresholding Segmentation

Input: Grayscale image I, threshold T
Output: Binary mask M
for each pixel p in I **do**
    if $I(p) \geq T$ **then**
        $M(p) \leftarrow 1$ ▷ Foreground
    else
        $M(p) \leftarrow 0$ ▷ Background
    end if
end for

Region Growing: Expands a region from a seed pixel by including neighboring pixels with intensity differences below a specified tolerance. Six tolerance values were analyzed:

$$R_1 = 0.01, \quad R_2 = 0.03, \quad R_3 = 0.05, \quad R_4 = 0.07, \quad R_5 = 0.10, \quad R_6 = 0.15.$$

Note. *For the experimental results on the image taken from* [**20**] *we employed a different set of parameters in order to enhance the clarity of the segmentation boundaries. Specifically, the following values were applied:*

$$R_1 = 0.15, \quad R_2 = 0.20, \quad R_3 = 0.25, \quad R_4 = 0.37, \quad R_5 = 0.40, \quad R_6 = 0.45.$$

These parameter choices were introduced to provide more distinct visual separation of the segmented regions and to facilitate a clearer comparison among the methods.

Algorithm 2 Region Growing

Input: Image I, seed pixel s, tolerance τ
Output: Binary mask M
Initialize M with zeros
Initialize queue Q with seed s
while Q not empty **do**
    Pop pixel p from Q
    if $M(p) = 0$ and $|I(p) - I(s)| < \tau$ **then**
        $M(p) \leftarrow 1$
        Add all neighbors of p to Q
    end if
end while

Watershed Segmentation: Treats the image as a topographic surface, where local minima define catchment basins. Gradient threshold factors tested:

$$W_1 = 0.01, \quad W_2 = 0.05, \quad W_3 = 0.10, \quad W_4 = 0.12, \quad W_5 = 0.15, \quad W_6 = 0.20.$$

Algorithm 3 Watershed Segmentation

Input: Image I, factor F
Output: Label image L
Compute gradient magnitude $G = \text{sobel}(I)$
Detect markers where $G < F \cdot \max(G)$
Apply watershed algorithm on G using markers
Output label image L

Fuzzy C-Means Clustering (FCM): Assigns membership degrees for each pixel to multiple clusters. The number of clusters tested:

$$C_2 = 2, \quad C_3 = 3, \quad C_4 = 4, \quad C_5 = 5, \quad C_6 = 6, \quad C_7 = 7.$$

Algorithm 4 Fuzzy C-Means Clustering

Input: Image I, number of clusters c, fuzziness m
Output: Label image L
Flatten image into vector
Apply FCM clustering algorithm
Assign each pixel to cluster with highest membership
Reshape labels to original image size

Feature Pyramid Network (FPN): Generates segmentation masks by applying a pre-trained FPN model to a 3-channel image and thresholding the output. Six threshold values were analyzed:

$$F_1 = 0.30, \quad F_2 = 0.40, \quad F_3 = 0.45, \quad F_4 = 0.50, \quad F_5 = 0.55, \quad F_6 = 0.60.$$

Note. *For the experimental results on the image taken from* [**20**] *we employed a different set of parameters in order to enhance the clarity of the segmentation boundaries. Specifically, the following values were applied:*

$$F_1 = 0.10, \quad F_2 = 0.14, \quad F_3 = 0.25, \quad F_4 = 0.30, \quad F_5 = 0.35, \quad F_6 = 0.40.$$

These parameter choices were introduced to provide more distinct visual separation of the segmented regions and to facilitate a clearer comparison among the methods.

Algorithm 5 FPN

Input: Grayscale image I, thresholds $\{F_1, F_2, F_3, F_4, F_5, F_6\}$
Output: Binary masks $\{M_1, M_2, M_3, M_4, M_5, M_6\}$
Convert I to 3-channel image I_{3ch}
Resize I_{3ch} to the input size of the FPN
Normalize I_{3ch} according to FPN requirements
Feed I_{3ch} into pre-trained FPN to obtain output O
Apply sigmoid to O to obtain probability map P
Resize P to the original image size
for $i = 1$ **to** 6 **do**
    $M_i \leftarrow (P > F_i)$ ▷ Generate binary mask for threshold F_i
    Display M_i in subplot with title F_i
end for

ε -Clustering: A graph-based approach where neighboring pixels are connected if their intensity difference does not exceed ε. Six ε values tested:

$$E_1 = 0.01, \quad E_2 = 0.03, \quad E_3 = 0.05, \quad E_4 = 0.07, \quad E_5 = 0.10, \quad E_6 = 0.15.$$

Algorithm 6 ε- Clustering

Input: Image I, threshold ε
Output: Label image L
Create graph G with pixels as nodes
for each pair of neighboring pixels (p, q) **do**
    if $|I(p) - I(q)| \leq \varepsilon$ **then**
        Add edge between p and q
    end if
end for
Compute connected components of G
Assign unique labels to each component
Output label image L

Each parameter set was applied separately and the resulting segmentation masks are visualized in Figures 7 and 8 . This systematic evaluation allows a direct

comparison of the sensitivity of each method to its key parameter and demonstrates how parameter selection influences the final segmentation outcome.

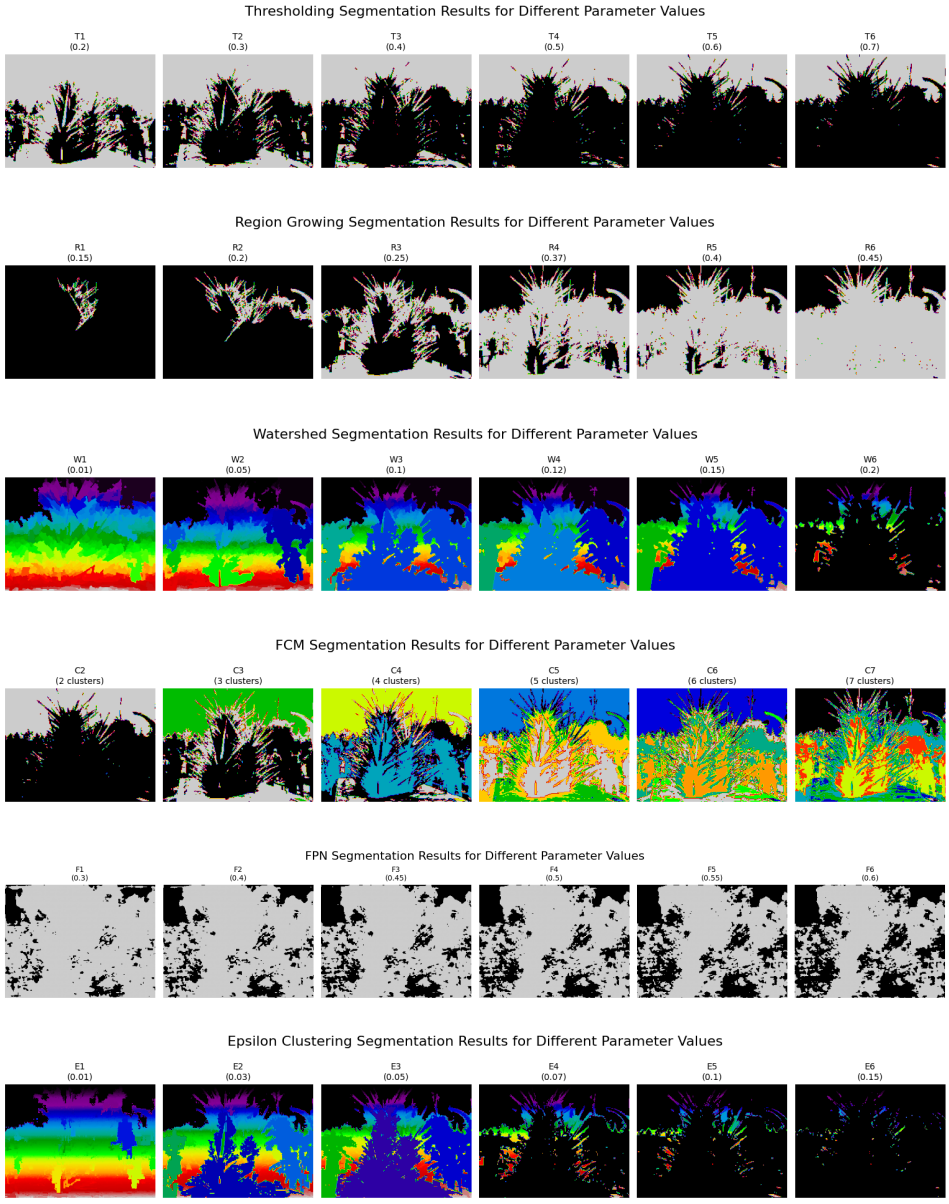

Figure 7: Segmentation results on image [**20**] obtained using five different methods: Thresholding (T_1–T_6), Region Growing (R_1–R_6), Watershed (W_1–W_6), FCM (C_2–C_7), FPN (F_1–F_6), and ε-clustering (E_1–E_6).

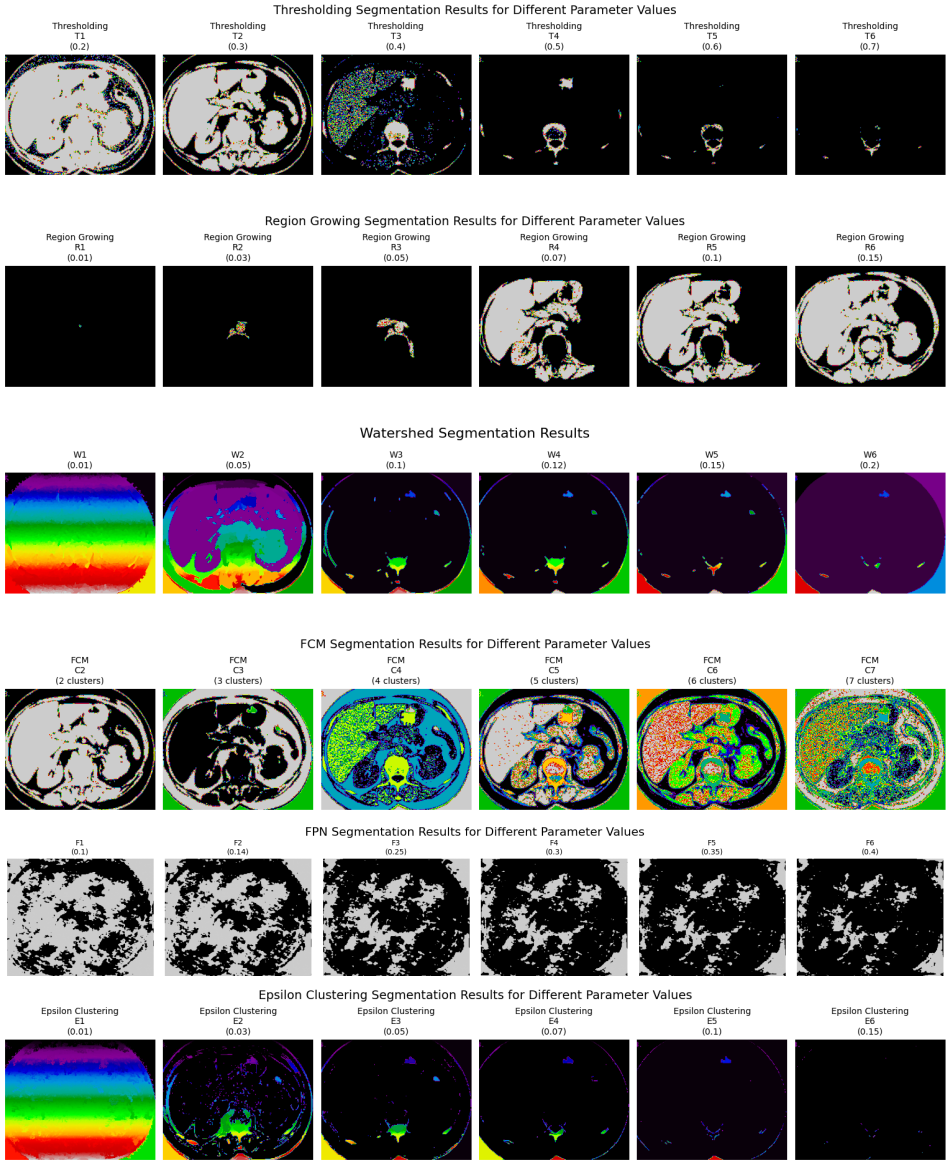

Figure 8: Segmentation results on a sample CT abdomen image [**9**] obtained using five different methods: Thresholding (T_1–T_6), Region Growing (R_1–R_6), Watershed (W_1–W_6), FCM (C_2–C_7), FPN (F_1–F_6), and ε-clustering (E_1–E_6). Each subfigure illustrates how varying key parameters affects segmentation quality, boundary precision, and spatial coherence of the regions of interest.

After presenting a general description of segmentation techniques, we extend

the analysis by examining their integration with the ε-clustering approach. In this combined framework each segmentation method is applied with a selected set of parameters. The resulting segmentation masks are subsequently processed through ε-clustering, a graph-based technique in which pixels are represented as nodes and edges are established whenever the difference in intensity values between neighboring pixels does not exceed a predefined threshold ε. This step provides an additional partitioning of the segmented image into connected components, allowing us to capture local homogeneity in the intensity domain.

The parameter sets investigated for each method are the following:

$$\begin{aligned} T &= \{0.2, 0.3, 0.35, 0.4, 0.5, 0.55\}, \\ R &= \{0.15, 0.18, 0.22, 0.25, 0.30, 0.35\}, \\ W &= \{0.01, 0.05, 0.10, 0.12, 0.15, 0.17\}, \\ C &= \{2, 3, 4, 5, 6, 7\}, \\ F &= \{0.3, 0.35, 0.40, 0.45, 0.50, 0.55\}. \end{aligned}$$

Here, T denotes the threshold values used in simple binarization. Lower thresholds generally preserve faint structures but may introduce additional background noise, while higher thresholds suppress noise at the cost of omitting subtle details. The parameters R represent tolerance values for region growing, where smaller tolerances restrict the expansion of regions to highly homogeneous areas, and larger tolerances enable broader inclusion of surrounding pixels. For Watershed segmentation, W denotes gradient-based thresholds that determine the sensitivity of catchment basin detection: lower values generate finer partitions with possible over-segmentation, whereas higher values yield coarser delineations. In the case of fuzzy C-means clustering, C corresponds to the number of clusters imposed on the image, influencing the granularity of the partitioning and the distribution of membership degrees across the regions.

Following the initial segmentation all obtained masks were processed with ε-clustering using a fixed value of $\varepsilon = 0.05$. This parameter was selected to balance sensitivity to intensity differences while avoiding excessive fragmentation of regions. The application of ε-clustering ensures that the results highlight graph-based connected components derived from the output of each segmentation method, thereby providing a unified framework for comparing their performance under varying parameter conditions.

This experimental design enables us to investigate how the selection of segmentation parameters directly affects the structure of ε-clusters. By systematically combining classical segmentation with graph-based clustering we obtain a more refined perspective on the delineation of regions of interest. The final results visualized in Figures 9 and 10 illustrate the sensitivity of each method to its parameters and demonstrate how the integration with ε-clustering enhances the interpretability of the segmentation outcomes.

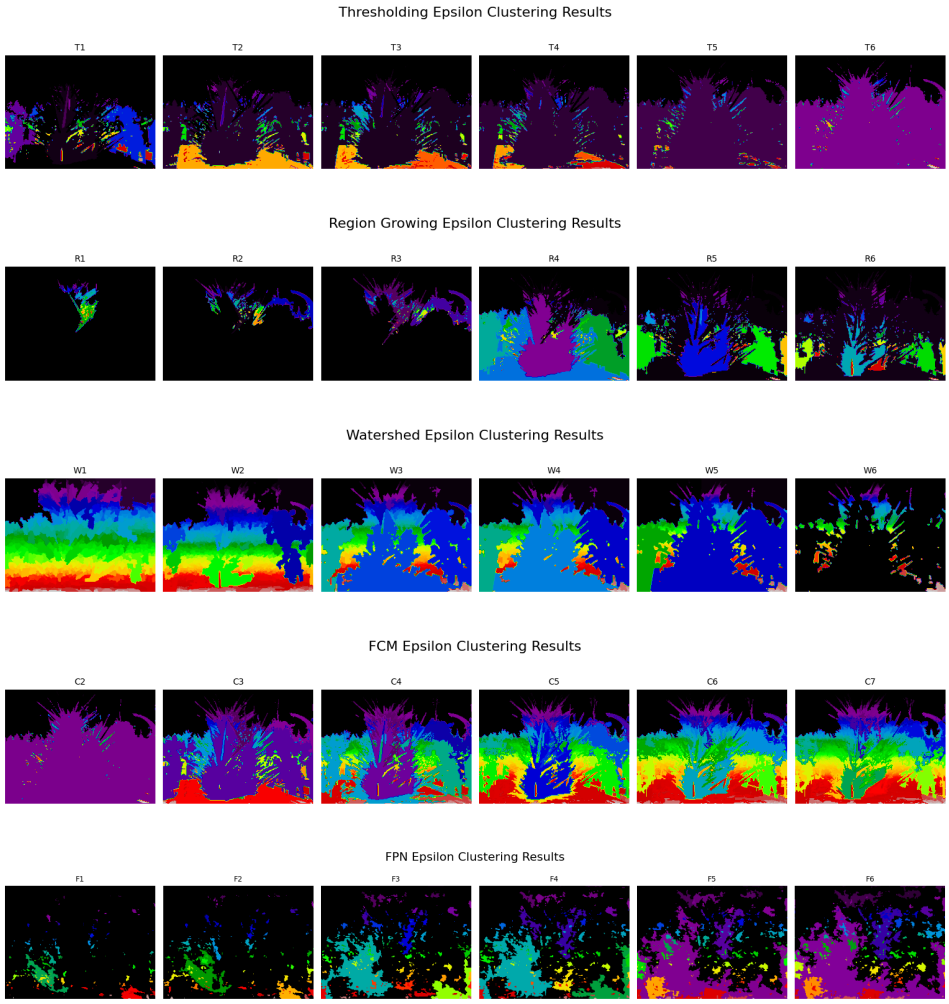

Figure 9: Segmentation results on image [**20**] obtained using different methods: Thresholding (T_1–T_6), Region Growing (R_1–R_6), Watershed (W_1–W_6), FCM (C_2–C_7), and FPN (F_1–F_6).

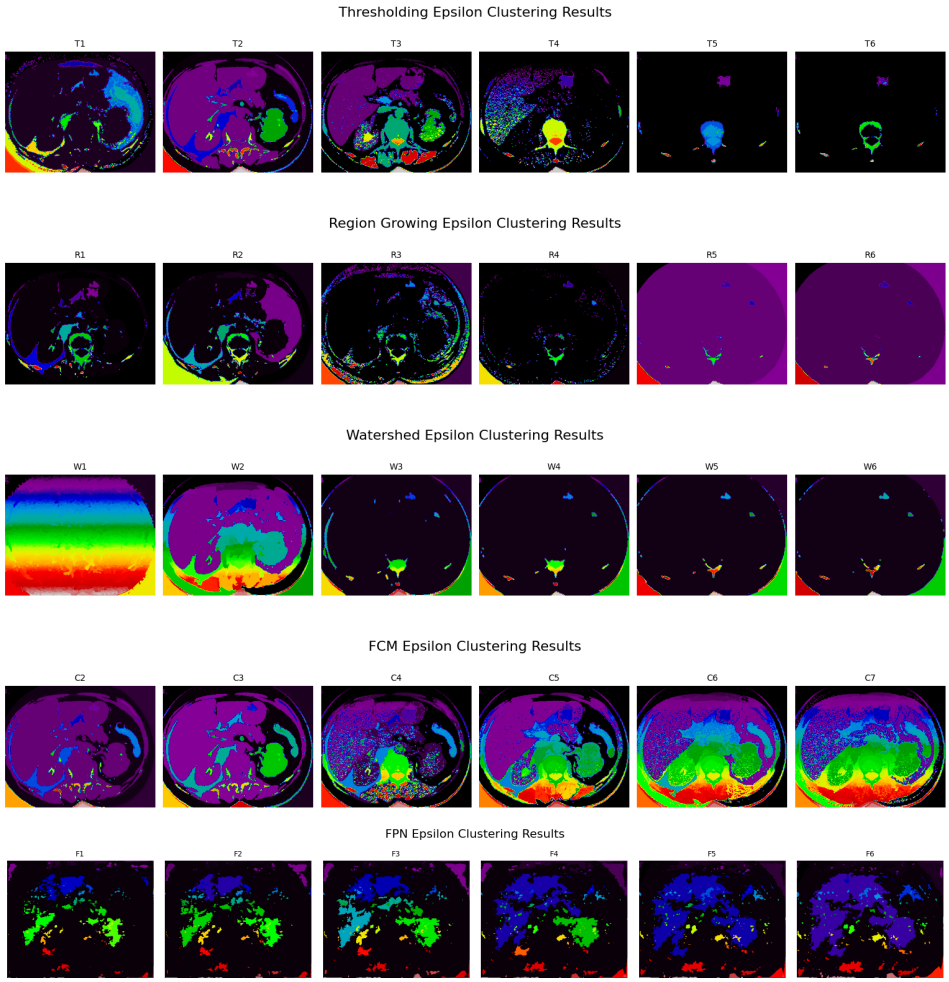

Figure 10: Segmentation results on a sample CT abdomen image [**9**] obtained using different methods: Thresholding (T_1–T_6), Region Growing (R_1–R_6), Watershed (W_1–W_6), FCM (C_2–C_7), and FPN (F_1–F_6).

In the following, based on the obtained segmentation figures, we present and analyze the evaluation metrics that allow quantitative assessment of segmentation quality for different methods and parameters. The results are presented in Table 1 and Table 2, where the Dice coefficient, Jaccard index, Davies-Bouldin index, Calinski-Harabasz index, and Silhouette coefficient were used. These metrics provide insight into segmentation accuracy with respect to the reference region, as well as cluster homogeneity and separation. For reference, Dice and Jaccard values close to 1 indicate high agreement with the reference region, while values below 0.5 suggest poor overlap. Davies-Bouldin indices range from 0 to ∞, where lower

values indicate more coherent clusters. Calinski-Harabasz indices generally increase with well-separated clusters, whereas Silhouette coefficients vary from -1 to 1: values near 1 indicate clearly defined clusters, values around 0 indicate overlapping or indistinct clusters, and negative values suggest fragmented or poorly separated clusters.

Table 1: Segmentation results for different methods and parameters for Figure 7

Method	Param	Dice	Jaccard	Davies-Bouldin	Calinski-Harabasz	Silhouette
Thresholding	0.20	1.00	1.00	0.68	2197.41	0.31
Thresholding	0.30	1.00	1.00	0.57	5633.21	0.54
Thresholding	0.40	1.00	1.00	0.44	11282.11	0.68
Thresholding	0.50	1.00	1.00	0.33	18003.61	0.76
Thresholding	0.60	1.00	1.00	0.27	20537.54	0.79
Thresholding	0.70	1.00	1.00	0.24	18635.75	0.78
Region Growing	0.15	1.00	1.00	36.25	0.08	-0.20
Region Growing	0.20	1.00	1.00	8.40	3.25	-0.19
Region Growing	0.25	1.00	1.00	3.52	120.23	0.13
Region Growing	0.37	1.00	1.00	1.19	1529.74	0.49
Region Growing	0.40	1.00	1.00	0.73	3233.04	0.60
Region Growing	0.45	1.00	1.00	0.26	10482.64	0.73
Watershed	0.01	N/A	N/A	60.59	473.47	-0.56
Watershed	0.05	N/A	N/A	243.93	184.32	-0.67
Watershed	0.10	N/A	N/A	245.20	197.59	-0.73
Watershed	0.12	N/A	N/A	507.40	251.34	-0.67
Watershed	0.15	N/A	N/A	117.12	288.81	-0.51
Watershed	0.20	N/A	N/A	89.88	424.68	-0.36
FCM	2	1.00	1.00	0.27	20539.30	0.78
FCM	3	N/A	N/A	0.46	27649.55	0.68
FCM	4	N/A	N/A	0.47	32835.32	0.65
FCM	5	N/A	N/A	0.47	42285.37	0.65
FCM	6	N/A	N/A	0.47	50904.18	0.64
FCM	7	N/A	N/A	0.47	58610.40	0.64
FPN	0.30	1.00	1.00	4.58	2.62	-0.27
FPN	0.35	1.00	1.00	4.52	2.59	-0.27
FPN	0.40	1.00	1.00	4.91	1.88	-0.27
FPN	0.45	1.00	1.00	4.98	1.80	-0.27
FPN	0.50	1.00	1.00	4.98	1.63	-0.27
FPN	0.55	1.00	1.00	5.19	1.45	-0.27
Epsilon Clustering	0.01	N/A	N/A	25131.29	7795.07	-0.34
Epsilon Clustering	0.03	N/A	N/A	14.77	285.80	-0.58
Epsilon Clustering	0.05	N/A	N/A	15252.84	213.38	-0.72
Epsilon Clustering	0.07	N/A	N/A	23.72	111.24	-0.79
Epsilon Clustering	0.10	N/A	N/A	16.38	119.08	-0.86
Epsilon Clustering	0.15	N/A	N/A	11.57	163.40	-0.88

Table 1 shows the segmentation metrics applied to the plant image. The Thresholding method achieves perfect agreement with the reference segmentation for all observed thresholds, with Dice and Jaccard values of 1.00. Increasing the threshold from 0.20 to 0.60 results in a decrease of the Davies-Bouldin index, while the Calinski-Harabasz and Silhouette indices increase, indicating improved cluster homogeneity and clear separation of regions. The most favorable results are observed for thresholds between 0.50 and 0.60. The Region Growing method shows that low thresholds lead to fragmented regions, reflected by high Davies-Bouldin values and negative Silhouette coefficients, while increasing thresholds to 0.37–0.45 results in coherent clusters and positive Silhouette indices up to 0.73, with low Davies-Bouldin values and high Calinski-Harabasz indices. The Watershed method is highly sensitive to the threshold, with negative Silhouette values and high Davies-

Bouldin indices for all observed thresholds, indicating fragmented regions. FCM with 2 clusters provides the best results, with Dice and Jaccard values of 1.00, low Davies-Bouldin index, and high Silhouette coefficient, whereas increasing the number of clusters reduces cluster coherence and segmentation quality. The ε-clustering method is highly sensitive to the ε parameter, small values lead to fragmentation, while larger values merge different regions thus resulting in negative Silhouette indices and high Davies-Bouldin values.

Table 2: Segmentation results for different methods and parameters for Figure 8

Method	Param	Dice	Jaccard	Davies-Bouldin	Calinski-Harabasz	Silhouette
Thresholding	0.20	1.00	1.00	0.59	10745.73	0.57
Thresholding	0.30	1.00	1.00	0.49	13003.07	0.64
Thresholding	0.40	1.00	1.00	0.80	2279.75	0.28
Thresholding	0.50	1.00	1.00	0.54	1349.21	0.58
Thresholding	0.60	1.00	1.00	0.45	863.04	0.66
Thresholding	0.70	1.00	1.00	0.32	524.26	0.73
Region Growing	0.01	1.00	1.00	1.37	3.47	-0.31
Region Growing	0.03	1.00	1.00	1.24	404.86	-0.09
Region Growing	0.05	1.00	1.00	1.00	1342.90	0.16
Region Growing	0.07	1.00	1.00	0.91	2106.29	0.28
Region Growing	0.10	1.00	1.00	0.71	4263.87	0.52
Region Growing	0.15	1.00	1.00	0.79	4303.80	0.50
Watershed	0.01	N/A	N/A	262.31	111.92	-0.65
Watershed	0.05	N/A	N/A	300.80	137.84	-0.63
Watershed	0.10	N/A	N/A	275537.70	213.15	-0.56
Watershed	0.12	N/A	N/A	127.09	109.96	-0.67
Watershed	0.15	N/A	N/A	75.14	129.27	-0.71
Watershed	0.20	N/A	N/A	21.20	241.14	-0.67
FCM	2	1.00	1.00	0.49	14262.73	0.66
FCM	3	N/A	N/A	0.31	17820.37	0.72
FCM	4	N/A	N/A	0.56	18024.81	0.60
FCM	5	N/A	N/A	0.43	32810.04	0.67
FCM	6	N/A	N/A	0.46	34797.97	0.63
FCM	7	N/A	N/A	0.49	34406.00	0.59
FPN	0.10	1.00	1.00	1.39	29.73	0.30
FPN	0.14	1.00	1.00	1.39	29.73	0.30
FPN	0.25	1.00	1.00	1.27	31.98	0.36
FPN	0.30	1.00	1.00	1.19	33.61	0.38
FPN	0.35	1.00	1.00	1.19	33.61	0.38
FPN	0.40	1.00	1.00	1.19	33.61	0.38
Epsilon Clustering	0.01	N/A	N/A	146547.64	1252.45	-0.49
Epsilon Clustering	0.03	N/A	N/A	156805.12	243.09	-0.79
Epsilon Clustering	0.05	N/A	N/A	86199.04	28.33	-0.85
Epsilon Clustering	0.07	N/A	N/A	20.61	32.92	-0.87
Epsilon Clustering	0.10	N/A	N/A	12.97	71.87	-0.87
Epsilon Clustering	0.15	N/A	N/A	7.81	25.68	-0.87

Table 2 presents the segmentation metrics applied to the medical image, where precise identification of regions of interest is crucial. The Thresholding method again shows perfect agreement with the reference segmentation, with optimal thresholds between 0.30 and 0.70, where Davies-Bouldin indices are low and Calinski-Harabasz and Silhouette indices are high, confirming clear separation and homogeneity of regions. Region Growing performs well for thresholds from 0.05 to 0.15, low values lead to fragmentation and negative Silhouette indices, while medium thresholds enable precise and stable segmentation of the medical regions of interest. The Watershed method is highly sensitive to threshold with negative Silhouette values and high Davies-Bouldin indices, indicating cluster fragmentation

and low segmentation reliability. FCM with 2 clusters provides the best results with high values for all evaluation metrics while increasing the number of clusters reduces the Silhouette index, indicating lower cluster homogeneity and potential fragmentation of regions of interest. ε-clustering method is highly sensitive to the epsilon parameter, small values cause fragmentation, while larger values merge different regions thus resulting in negative Silhouette indices and high Davies-Bouldin values.

Thresholding and FCM with two clusters are the most reliable methods for segmenting both plant and medical images, combining high precision with homogeneous and well-defined clusters. Region Growing provides good results for medium threshold values, whereas Watershed requires careful parameter tuning to achieve satisfactory segmentation.

The segmentation results presented in Tables 3 and 4 correspond to the foreground extraction of plant and medical images respectively. Compared to the previous results obtained with ε-clustering these methods exhibit improved consistency and more coherent clusters despite the relatively low Dice and Jaccard values. Thresholding consistently yields uniform segmentation across different parameter values with minimal variation in Davies-Bouldin and Calinski-Harabasz indices. Region Growing demonstrates a gradual improvement in cluster homogeneity as the parameter increases which is reflected in slightly higher Calinski-Harabasz indices and less negative Silhouette coefficients thus indicating reduced fragmentation. The Watershed method produces variable results with moderate Davies-Bouldin values and Silhouette coefficients, suggesting that the method captures the general structure of the foreground but still generates minor over-segmentation. FCM results are relatively stable across different cluster numbers, showing better cluster coherence and slightly higher Silhouette indices than in the previous ε-clustering experiments. Overall, these results indicate that the applied segmentation methods are more effective at extracting the foreground regions, providing more reliable and structured segmentation compared to the earlier ε-clustering approach, which exhibited significant fragmentation and poor cluster homogeneity.

FPN exhibits consistent performance across the tested parameter range, achieving high Dice and Jaccard scores, which indicate strong agreement with the manually prepared reference segmentation. Although the evaluation is conducted on a limited number of images, these results clearly illustrate the behavior of FPN as well as, more generally, other classical segmentation methods in identifying the main structures. Cluster-based indices such as Davies-Bouldin, Calinski-Harabasz, and Silhouette show moderate values, reflecting that FPN captures the primary regions effectively while producing moderately coherent local clusters. This stability across different thresholds and parameters demonstrates the reliability of FPN and provides valuable insights into the overall segmentation performance, highlighting its applicability even under varying conditions and for different types of images. Consequently, the observations made here can be considered indicative of the general behavior of the evaluated segmentation methods.

It should be noted that the evaluation in this study was conducted on a single

representative image for each scenario. While a manually annotated ground truth was not available, the chosen images provide clear structural features that allow for meaningful comparison of segmentation methods. This approach focuses on assessing the relative performance, stability across parameters, and the quality of clustering of each method, rather than establishing absolute quantitative metrics. The observed trends are consistent across different segmentation approaches, suggesting that even with a limited dataset, valuable insights into the behavior and robustness of the methods can be drawn. Future studies will extend this analysis to larger datasets with manually annotated ground truth to further validate the findings.

When considering the segmentation methods through the lens of ε-clustering, the results summarized in Tables 3 and 4 illustrate how each method behaves after additional graph-based processing. For the plant image (Table 3) the Dice and Jaccard indices are around 0.28, reflecting the fragmentation introduced by the ε-clustering procedure. Nevertheless, cluster-based indices such as Davies-Bouldin and Calinski-Harabasz indicate improved homogeneity and more clearly defined local clusters. Region Growing and FCM methods maintain stable performance across their respective parameter ranges, whereas Thresholding and Watershed exhibit greater sensitivity to parameter changes, reflecting their dependence on intensity and gradient thresholds. This approach allows finer structural details to emerge and provides a more organized representation of the segmented regions.

Similarly, for the medical image (Table 4), ε-clustering further subdivides the regions leading to lower Dice and Jaccard values around 0.14 while simultaneously enhancing the local coherence of clusters. Region Growing and FCM remain relatively stable, whereas Thresholding and Watershed show variability depending on the selected parameters. The negative Silhouette coefficients indicate a fine-grained subdivision of regions, which facilitates a more precise analysis of the internal structure of the image.

This analysis demonstrates that ε-clustering can serve as a valuable tool for evaluating classical segmentation methods, emphasizing local homogeneity and connectivity of regions. Although the overlap metrics slightly decrease due to fragmentation, the resulting clusters provide a more detailed and structured view of the segmentation thus allowing a deeper understanding of each method's behavior under varying parameter conditions.

Table 3: Segmentation results for different methods and parameters for Figure 9

Method	Parameter	Dice	Jaccard	Davies-Bouldin	Calinski-Harabasz	Silhouette
Thresholding	0.20	0.28	0.16	2.49	11.25	-0.70
Thresholding	0.30	0.28	0.16	2.01	14.51	-0.73
Thresholding	0.35	0.28	0.16	1.82	15.31	-0.73
Thresholding	0.40	0.28	0.16	2.20	16.79	-0.74
Thresholding	0.50	0.28	0.16	1.36	14.66	-0.75
Thresholding	0.55	0.28	0.16	1.79	20.24	-0.73
Region Growing	0.15	0.28	0.16	2.92	0.84	-0.44
Region Growing	0.18	0.28	0.16	2.93	3.20	-0.55
Region Growing	0.22	0.28	0.16	2.95	4.28	-0.60
Region Growing	0.25	0.28	0.16	2.42	42.33	-0.63
Region Growing	0.30	0.28	0.16	2.07	24.10	-0.66
Region Growing	0.35	0.28	0.16	2.07	17.19	-0.70
Watershed	0.01	0.28	0.16	1.09	207.12	-0.19
Watershed	0.05	0.28	0.16	0.89	52.82	-0.35
Watershed	0.10	0.28	0.16	0.96	30.59	-0.53
Watershed	0.12	0.28	0.16	0.97	34.34	-0.53
Watershed	0.15	0.28	0.16	1.27	15.69	-0.64
Watershed	0.17	0.28	0.16	1.41	3.63	-0.72
FCM	2	0.28	0.16	1.93	22.58	-0.72
FCM	3	0.28	0.16	2.14	13.70	-0.74
FCM	4	0.28	0.16	2.01	19.25	-0.66
FCM	5	0.28	0.16	2.12	14.80	-0.60
FCM	6	0.28	0.16	1.55	39.89	-0.51
FCM	7	0.28	0.16	1.38	59.44	-0.43
FPN	0.30	0.28	0.16	0.90	18.52	0.03
FPN	0.35	0.28	0.16	0.90	15.85	0.02
FPN	0.40	0.28	0.16	0.91	13.21	0.02
FPN	0.45	0.28	0.16	0.91	13.21	0.02
FPN	0.50	0.28	0.16	0.90	12.09	0.02
FPN	0.55	0.28	0.16	0.90	12.09	0.02

Table 4: Segmentation results for different methods and parameters for Figure 10

Method	Parameter	Dice	Jaccard	Davies-Bouldin	Calinski-Harabasz	Silhouette
Thresholding	0.20	0.14	0.07	2.28	18.70	-0.79
Thresholding	0.30	0.14	0.07	2.76	35.98	-0.73
Thresholding	0.35	0.14	0.07	2.40	6.97	-0.82
Thresholding	0.40	0.14	0.07	1.63	1.57	-0.80
Thresholding	0.50	0.14	0.07	3.50	5.50	-0.66
Thresholding	0.55	0.14	0.07	1.56	3.11	-0.66
Region Growing	0.15	0.14	0.07	2.30	13.38	-0.78
Region Growing	0.18	0.14	0.07	2.55	40.55	-0.72
Region Growing	0.22	0.14	0.07	1.57	9.50	-0.76
Region Growing	0.25	0.14	0.07	1.94	21.79	-0.77
Region Growing	0.30	0.14	0.07	1.24	142.55	-0.58
Region Growing	0.35	0.14	0.07	1.36	119.25	-0.57
Watershed	0.01	0.14	0.07	0.83	159.96	-0.12
Watershed	0.05	0.14	0.07	2.06	24.41	-0.62
Watershed	0.10	0.14	0.07	1.06	16.06	-0.73
Watershed	0.12	0.14	0.07	1.07	18.78	-0.70
Watershed	0.15	0.14	0.07	1.08	27.51	-0.68
Watershed	0.17	0.14	0.07	1.08	47.66	-0.64
FCM	2	0.14	0.07	3.21	45.95	-0.72
FCM	3	0.14	0.07	2.97	39.16	-0.75
FCM	4	0.14	0.07	3.18	8.24	-0.75
FCM	5	0.14	0.07	2.53	16.63	-0.72
FCM	6	0.14	0.07	3.18	14.77	-0.64
FCM	7	0.14	0.07	2.85	10.88	-0.57
FPN	0.30	0.14	0.07	10.32	0.61	-0.27
FPN	0.35	0.14	0.07	10.09	0.61	-0.27
FPN	0.40	0.14	0.07	9.84	0.63	-0.27
FPN	0.45	0.14	0.07	9.25	0.60	-0.27
FPN	0.50	0.14	0.07	9.00	0.61	-0.27
FPN	0.55	0.14	0.07	9.29	0.54	-0.28

5. RESULTS

Our experiments show that simultaneous utilizing ε-clustering with fuzzy graphs leads to a noticeable improvement over the initial segmentation results. In preliminary tests on a general image this approach was able to better preserve the structure of regions while reducing noise and fragmented areas. Standard metrics including the Dice coefficient and Jaccard index consistently confirmed the method's enhanced performance.

Applying the same approach to medical images which are central to our study produced promising outcomes. The ε-clustering method successfully highlighted the regions of interest that were not fully captured by the initial segmentation alone. By using fuzzy graphs the algorithm could consider both local pixel similarity and the overall structure of the image, resulting in more accurate and coherent segmentation. This demonstrates that our approach is not only effective, but also adaptable to the complexities of medical imaging.

Hence, the results indicate that integrating initial segmentation with ε-clustering through fuzzy graphs offers a reliable and practical method for improving image analysis. The method handles variations in image quality and content effectively, and it consistently delivers high-quality segmentations.

6. CONCLUSION

The proposed approach has demonstrated effectiveness in the segmentation of medical images, confirming its capability to accurately identify relevant regions of interest. Initial testing was conducted on a standard image to evaluate its general applicability followed by application to a medical image relevant to this study, where the results showed a substantial improvement in segmentation accuracy compared to baseline methods. The obtained results indicate consistency and reliability of the method, suggesting that it can be applied to more complex medical data with minimal deviations and clearly defined regions.

It is important to emphasize that, although the experiments were initially performed on a limited number of images, the method itsself shows potential for broader application in medical image analysis. Further research could focus on evaluating the approach on larger image datasets which would allow additional validation and identification of potential limitations in various scenarios. Additionally, optimization and adaptation of the method for different types of medical images could lead to further enhancement of segmentation accuracy, as ell as its reliability.

Acknowledgements. This work is partially supported by the Science Fund of the Republic of Serbia, Grant No. 7632, Project "Mathematical Methods in Image Processing under Uncertainty" (MaMIPU), and also by the Ministry of Science,

Technological Development and Innovation of the Republic of Serbia under contract numbers: 451-03-137/2025-03/200156 and 451-03-137/2025-03/200103.

REFERENCES

1. B. Akyildiz, C. Ozcan & İ.R. Karaş: *Graph Cuts in Image Segmentation: A Review.* in: G. Mammadova et al. (Eds.): Proceedings of the 2nd International Conference on Information Technologies and Their Applications (ITTA 2024), Part 3, pp.1-15, Baku, Azerbaijan (2024).
2. K. Amrulloh, T.H. Pudjiantoro, P.N. Sabrina & A.I. Hadiana: *Comparison Between Davies-Bouldin Index and Silhouette Coefficient Evaluation Methods in Retail Store Sales Transaction Data Clusterization Using K-Medoids Algorithm.* Proceedings of the 3rd South American International Industrial Engineering and Operations Management Conference, Asunción, Paraguay, July 19–21, (2022) 1952-1961.
3. J. Bertels, T. Eelbode, M. Berman, D. Vandermeulen, F. Maes, R. Bisschops & M. B. Blaschko: *Optimizing the Dice Score and Jaccard Index for Medical Image Segmentation: Theory & Practice.* IEEE Transactions on Medical Imaging, **39** (2020), no. 6, 1854–1866.
4. P. Bhattacharya & S. Suraweera: *An algorithm to compute the supremum of max-min powers and a property of fuzzy graphs.* Pattern Recognition Letters, **12** (1991), no. 7, 413–420.
5. R. C. González & R. E. Woods: *Digital Image Processing.* 4th Edition, Pearson, (2018).
6. L. Grady: *Random Walks for Image Segmentation.* IEEE Transactions on Pattern Analysis and Machine Intelligence, **28** (2006), no. 11, 1768–1783.
7. G. M. Hadi & N. H. Salman: *Image Segmentation Based on Single Seed Region Growing Algorithm.* ZANCO Journal of Pure and Applied Sciences, **28** (2016), no. 2, 120–126.
8. R.J. Hemalatha, T.R. Thamizhvani, A.J.A. Dhivya, J.E. Joseph, B. Babu & R. Chandrasekaran: *Active Contour Based Segmentation Techniques for Medical Image Analysis.* in: R. Koprowski (Ed.): Medical and Biological Image Analysis, Chapter 2, 17-34, IntechOpen, London (2018).
9. I. Ibrišimović, B. Iričanin, N. Milosavljević, Lj. Nedović & N. Ralević: *Fuzzy Numbers and Analysis of Radiological Images.* In: Intelligent and Fuzzy Systems: Intelligence and Sustainable Future, Proceedings of the 5^{th} INFUS 2023 Conference, Volume 2 (2023), pp. 108-115, LNNS, volume 759, Springer.
10. I. Ibrišimović, N. Ralević, B. Iričanin & V. Ilić: *Integrated Techniques for Radiological Image Analysis Using Graphs and Computational Methods.* In: D. Karabegović (Ed.) *New Technologies, Development and Application* 8^{th} NT 2025. Lecture Notes in Networks and Systems, vol. 1483. Springer, Cham, 2025, pp. 85–92. https://doi.org/10.1007/978-3-031-68392-3_9.
11. S. Jardim, J. António & C. Mora: *Image thresholding approaches for medical image segmentation - short literature review.* Procedia Computer Science, **219** (2023) 1485–1492.

12. S. V. Kasmir Raja, A. S. Khadir & S. S. R. Ahamed: *Novel Graph Based Method for Image Segmentation.* Journal of Theoretical and Applied Information Technology, **78** (2010), no. 15, 26–30.

13. A. Koundal, S. Budhiraja & S. Agrawal: *Medical Image Segmentation using Enhanced Feature Weight Learning Based FCM Clustering.* Biomedical & Pharmacology Journal, **17** (2024), no. 4, 2661–2672.

14. O. Lézoray & L. Grady (Eds.): *Image Processing and Analysis with Graphs: Theory and Practice.* CRC Press, (2012).

15. G. Liu: *A New Index for Clustering Evaluation Based on Density Estimation.* arXiv preprint arXiv:2207.01294v4 [cs.LG], 17 Jun (2024).

16. A.R. Mamat, F.S. Mohamed, M.A. Mohamed, N.M. Rawi & M.I. Awang: *Silhouette index for determining optimal k-means clustering on images in different color models.* International Journal of Engineering & Technology, **7**(2.14) (2018) 105–109.

17. N.S. Milosavljević, N.M. Ralević, B.D. Iričanin, D. Ćebić & I. Ibrišimović: *Determining the Optimal Number of Characteristic Vectors in Medical Digital Images.* In: Djrodje Jovanović at all. (Ed.B.), Book of Proceedings of The 3rd International Conference on Advances in Science and Technology (COAST 2024), Herceg Novi, Montenegro, 29 May–1 June 2024, p. 261-267.

18. J. N. Mordeson & P. S. Nair: *Fuzzy Graphs and Fuzzy Hypergraphs.* Studies in Fuzziness and Soft Computing (STUDFUZZ), Volume 46, Physica verlag, Heidelberg (2000).

19. N. Ralević, I. Ibrišimović, M. Paunović, B. Iričanin & T. Došenović: *Comparison of the Performance of a Fuzzy Algorithms for Removing Noise.* In: A. Abraham et al. (Eds.) *Intelligent and Fuzzy Systems.* 7^{th} INFUS 2025. Lecture Notes in Networks and Systems, vol. 1529. Springer, Cham, 2025, pp. 672–680. https://doi.org/10.1007/978-3-031-71399-6_67.

20. N.M. Ralević, B.D. Iričanin & D. Ćebić: *Pseudo-Linear Combination of Fuzzy Metrics.* Publications de l'Institut Mathematique, Nouvelle Serie, **116** (130) (2024), 35–53. DOI: https://doi.org/10.2298/PIM2430035R

21. N.M.Ralević, M. Paunović & B.Iričanin: *Fuzzy metric space and applications in image processing.* Math. Montisnigri, **48** (2020), 103-117.

22. M. Rempfler: *Graph Inference in Biomedical Image Analysis.* Ph.D. Dissertation, Faculty of Computer Science, Technical University of Munich, (2018).

23. O. Ronneberger, P. Fischer & T. Brox: *U-Net: Convolutional Networks for Biomedical Image Segmentation.* Computer Science Department and BIOSS Centre for Biological Signalling Studies, University of Freiburg, Germany, (2015).

24. S. Sangeetha: *A Study on Fuzzy Graph Theory and Its Applications.* Journal of algebraic statistics, **13** (2022), no. 3, 3877–3882.

25. M. L. Seghier: *Image Segmentation Evaluation With the Dice Index: Methodological Issues.* International Journal of Imaging Systems and Technology, **34** (2024), no.6, 34: e23203, 1-6.

26. S.A. Shaban & W.A.M. AlJawher: *K-Means Clustering Algorithm for Medical Images.* International Journal of Advances in Engineering and Management (IJAEM), **4** (2022), no. 11, 826–831.

27. H. Sun, S. Yang, L. Chen, P. Liao, X. Liu, Y. Liu & N. Wang: *Brain tumor image segmentation based on improved FPN.* BMC Medical Imaging, 23:172, (2023). DOI: 10.1186/s12880-023-01131-1.

28. R. Szeliski: *Computer Vision: Algorithms and Applications.* Springer, (2010).

29. L. Vincent & P. Soille: *Watersheds in Digital Spaces: An Efficient Algorithm Based on Immersion Simulations.* IEEE Transactions on Pattern Analysis and Machine Intelligence, **13** (1991), no. 6, 583–598.

30. S. Wang, M. Lin, T. Ghosal, Y. Ding & Y. Peng: *Knowledge Graph Applications in Medical Imaging Analysis: A Scoping Review.* The University of Texas at Austin, Population Health Sciences, Weill Cornell Medicine, and Institute of Formal and Applied Linguistics, Charles University, (2022).

31. Y. Wu & Q. Li: *The Algorithm of Watershed Color Image Segmentation Based on Morphological Gradient.* Sensors, **22** (2022), no. 21, Article 8202, 1-23, DOI: 10.3390/s22218202.

32. L. A. Zadeh: *Fuzzy Sets.* Information and Control, **8** (1965), no. 3, 338–353.

(Received 14.02.2025.)
(Revised 07.12.2025.)

Irma Ibrišimović
Department of Mathematics,
University of Tuzla,
Tuzla, Bosnia and Herzegovina
Faculty of Technical Sciences,
University of Novi Sad,
Novi Sad, Serbia
E-mail: *irma.ibrisimovic@untz.ba*
https://orcid.org/0000-0002-9361-0259

Nebojša M. Ralević
Department of Fundamental Disciplines,
Faculty of Technical Sciences,
University of Novi Sad,
Novi Sad, Serbia
E-mail: *nralevic@uns.ac.rs*
https://orcid.org/0000-0002-3825-9822

Bratislav D. Iričanin
Department of Applied Mathematics,
Faculty of Electrical Engineering,
University of Belgrade,
Belgrade, Serbia
Faculty of Mechanical and Civil Engineering in Kraljevo,
University of Kragujevac,
E-mail: *iricanin@etf.rs*
https://orcid.org/0000-0001-7457-7716

Andrija Blesić
Department of Fundamental Disciplines,
Faculty of Technical Sciences,
University of Novi Sad,
Novi Sad, Serbia
E-mail: *andrija.blesic@uns.ac.rs*
https://orcid.org/0000-0003-3814-7254